ADVANCED MATERIALS TECHNOLOGIES
www.advmattechnol.de

A Degradable Device for Sustainable Capillary Blood Sampling

*Nicole Zoratto, Hanna Krupke, Valeria Mantella, Daniel Gao, David Klein Cerrejon, and Jean-Christophe Leroux**

Capillary blood sampling plays a crucial role in diagnostic decentralization, yet most microsampling devices remain expensive, limiting their use mainly to developed countries. To improve accessibility, a cost-effective silicone device capable of extracting small volumes of capillary blood in vivo was previoulsy developed by our group. However, the use of non-degradable materials poses limitations, especially in resource-limited settings with inadequate waste disposal infrastructure. Herein, a nearly fully degradable microsampling prototype is reported. The device body is fabricated using digital light processing 3D printing with tailored poly(ε-caprolactone-co-D,L-lactide). This device yields negative pressure and adhesion strength comparable to the original prototype, although it requires greater manual compression. In vitro, it collects ≈670 µL of porcine whole blood, matching the volume drawn by the silicone counterpart. The device is equipped with magnesium microneedle blades coated with poly(ε-caprolactone) to enhance blood stability. Degradation studies show complete disintegration of poly (ε-caprolactone-co-D,L-lactide) under composting conditions within 60 days, and near-complete degradation of magnesium blades in aqueous buffer within 40 days. Preliminary hemolysis assays confirm blood compatibility of both the 3D-printed device and coated microneedles, with sample quality preserved for up to 3 h. Altogether, these findings highlight the potential of this degradable prototype as a sustainable alternative for capillary blood collection.

1. Introduction

Blood sampling is the primary diagnostic approach to assess the pathophysiological status of patients, with conventional venipuncture being the most commonly practiced technique.[1,2] Nevertheless, it has low acceptance, especially in children who frequently experience fear of needles, and imposes a financial burden on healthcare systems.[3,4] Indeed, this method requires well-trained phlebotomists, a long time for sample processing, and generates a large amount of biohazardous waste that is expensive to dispose of.[5] The requirements for safe venipuncture are especially challenging to meet in low- and middle-income countries (LMICs), where healthcare facilities may lack efficient waste disposal systems.[6,7] Even when the latter are available, the improper handling of needles and syringes remains a major concern.[8,9] As a result, needle-stick injuries (NSIs) are quite pronounced in these regions, largely resulting from scavenging at waste disposal sites and the manual sorting of hazardous medical waste.[10] These practices place waste handlers at immediate risk of NSIs and exposure to toxic or infectious materials, while also posing broader threats to environmental safety and public health.[11,12] Given these challenges, fingersticks combined with point-of-care (POC) devices may represent a useful alternative.[5] They enable rapid, on-site diagnostic testing in a friendly, non-clinical environment while generating a reduced amount of biohazardous waste and residual blood compared to venipuncture.[13,14] However, the use of non-degradable materials in these devices contributes to medical waste accumulation. Additionally, the high drop-to-drop variability associated with traditional fingerstick methods can compromise the accuracy and reliability of the POCs.[15,16] In this scenario, the recently developed microsampling devices (e.g., TAP® Micro, Tasso +, and Loop One) overcome some of these limitations by collecting larger blood volumes, thereby improving the reliability of analytical outcomes.[17–20] While their minimally invasive nature contributes to high patient acceptability, making them a compelling alternative to venipuncture, their relatively high cost may strictly limit their use to developed countries.

To make blood sampling a more user-friendly procedure, especially for children, and more accessible in LMICs while minimizing the risk of NSIs, we recently proposed a simple, open-source silicone prototype device capable of extracting ≈195 µL of capillary blood within minutes in vivo, providing sufficient volume for

N. Zoratto, H. Krupke, V. Mantella, D. Gao, D. Klein Cerrejon, J.-C. Leroux
Institute of Pharmaceutical Sciences
Department of Chemistry and Applied Biosciences
ETH Zürich
Zurich 8093, Switzerland
E-mail: jleroux@ethz.ch

The ORCID identification number(s) for the author(s) of this article can be found under https://doi.org/10.1002/admt.202501626

DOI: 10.1002/admt.202501626

diagnostic testing. Inspired by the anatomy of the sanguivorous leeches, the prototype exhibited strong skin adhesion and generated high negative pressure to facilitate blood withdrawal.[21]

All the above-mentioned sampling strategies rely on several non-degradable components, including syringes for venipuncture, plastic devices for capillary blood microsampling, spring-loaded mechanisms for fingersticks, as well as glass or plastic blood collection tubes and sharps.[10] Therefore, integrating degradable alternatives in healthcare holds immense potential for reducing the environmental impact of medical waste.[22–24] In this context, polyester-based degradable polymers have gained widespread use across various fields, including pharmaceuticals, orthopedics, cosmetics, and food packaging. Among them, poly(lactic acid) (PLA) stands out as the most widely utilized in medical devices, accounting for ≈40% of all biodegradable biopolymers.[25,26] Yet, PLA has some limitations, as its poor toughness can lead to device brittleness and failure under high-stress conditions.[27] As a result, copolymerization or blending with other polymers has been explored to optimize and tune PLA degradability and mechanical properties.[28,29] Similarly, there is also a growing interest in incorporating alternatives to traditional and non-degradable metals (e.g., stainless steel, titanium, etc.) for various biomedical applications. Among these, magnesium (Mg) has emerged as a promising candidate due to its biocompatibility, excellent mechanical properties, and biodegradability.[30,31] Indeed, in implants, Mg offers the advantage of eliminating the need for secondary surgeries associated with non-degradable materials, as its resorbable nature allows the implant to gradually degrade in vivo. However, Mg undergoes relatively rapid corrosion, accompanied by hydrogen gas release and a local increase in pH of the surrounding body fluids.[32] In capillary blood sampling, Mg degradation may adversely affect sample quality. To control and slow down corrosion, several strategies have been employed, including surface treatments, protective coatings, and alloy development. Among these, synthetic polymer-based coatings, such as poly(ε-caprolactone) (PCL), PLA, and poly(lactic-co-glycolic acid) (PLGA), have proven particularly effective, as they can modulate degradation kinetics while preserving the mechanical integrity of the implant over the intended functional period.[32]

Herein, we present an environmentally friendly version of our capillary microsampling device. For this purpose, tailored methacrylate poly(ε-caprolactone-co-D,L-lactide)s (poly(CL-LA)s) were used to fabricate the device body (suction cup and storage compartment) via 3D printing, enabling rapid prototyping as well as simple, decentralized production. Notably, similar to the previously reported silicone-based device, the elastic self-recovery of the material allows it to convert compression force into negative pressure, allowing blood extraction and collection into the device storage compartment.[21] The device design and wall thickness were optimized to ensure successful printing while achieving optimal negative pressure and adhesion strength for effective performance. In parallel, Mg blades with an optimized thickness were incorporated in the system, and their piercing efficacy was evaluated ex vivo. Thereafter, the blood compatibility of the device components was assessed, along with the degradation profile of the 3D-printed body under composting conditions and the Mg microneedles (MNs) in aqueous buffer. To improve stability in whole blood, Mg MNs were subsequently coated with PCL. Finally, the fully assembled prototype was tested ex vivo to determine whether the MN penetration depth in porcine skin was suitable for reaching the capillary network.

2. Results and Discussion

2.1. Prototype Design

The blood microsampling device operates by generating negative pressure through the elastic self-recovery of the material, thereby allowing blood collection and storage (**Figure 1A**). As previously described, the bioinspired device consists of: I) a concealed MN patch designed for minimal invasiveness, efficient skin penetration, and rapid wound healing; II) a suction cup that ensures a secure seal with the skin; and III) a storage compartment for liquid blood collection (Figure 1B). The operating principle is shown in Figure 1A. The device is manually compressed to deploy the MN patch and applied to the target body site. Upon attachment, the MNs puncture the skin, and the subsequent elastic recovery of the material following compression generates the negative pressure required to assist blood sampling.[21]

To address a key challenge in LMICs, we developed an almost fully degradable version of the blood microsampling device (Figures 1C-E). Digital light processing (DLP) was employed to fabricate the degradable device, as it enables rapid screening of different materials and precise tuning of the system's dimensions (size, shape, and wall thickness) to achieve the targeted negative pressure, while also ensuring high-resolution fabrication (Figure 1C). For the MN patch, Mg was selected due to its excellent mechanical properties and the ability to produce high-resolution features via nitrogen laser cutting (Figure 1D). Additionally, fused deposition modeling (FDM) with a compostable PLA filament was used to fabricate both the MN holder and the adapter, ensuring the degradability of nearly all device components, with the exception of the electrocardiogram adhesive (ECG) tape used for skin adhesion (Figures 1B–E).

2.2. Resin Selection for Device Fabrication Via DLP 3D Printing

Dual-polymer inks composed of high and low molecular weight (MW) blends of poly(CL-LA) have shown promise for the 3D printing of bioresorbable elastomers with mechanical properties closely resembling those of silicone.[29,33] Indeed, this dual-MW blending approach enables the fabrication of structures that combine the enhanced strength of densely cross-linked short polymer chains with the excellent elasticity of long, flexible chains. Moreover, by adjusting the MW and the blend ratios of the copolymers, both mechanical performance and degradation rate can be precisely tuned.[29,33,34]

Building on these findings, low-MW linear (number-average molecular weight ($M_{n\,NMR}$) ≈560 g mol^{-1}) and high-MW star-shaped ($M_{n\,NMR}$ ≈15 000 g mol^{-1}) random copolymers of CL and LA were synthesized via ring-opening polymerization (ROP) (Figures S1–S5 and Table S1, Supporting Information). The resulting copolymers were functionalized with methacrylate groups to make them photocurable and suitable for light-based 3D printing, achieving methacrylation degrees of ≈50% and 95% for the high- and low-MW poly(CL-LA), respectively

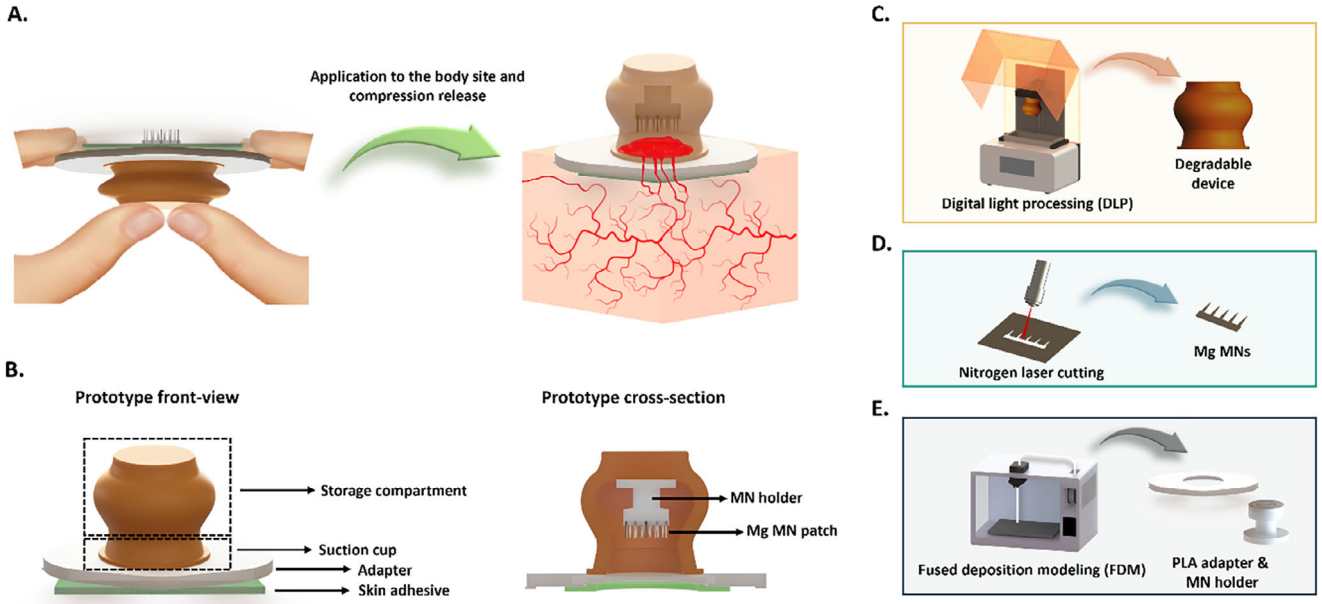

Figure 1. Schematic overview of the degradable blood microsampling device and its working principle. A) Operating principle of the degradable microsampling device. Manual compression of the device deploys the MNs, which create small skin punctures upon application. The subsequent release of the compression force creates negative pressure, required for capillary blood collection within the device. B) Front and cross-sectional views of the fully assembled degradable prototype, highlighting the different components. C) The device body was fabricated using DLP with a customized photocurable resin. D) Mg MN blades were manufactured via nitrogen laser cutting. E) A PLA holder, for MN embedding, and adapter were fabricated using FDM with commercial PLA filament.

(Figures S3–S5, Supporting Information). Three different resin formulations— R1, R2, and R3— were prepared by mixing different ratios of high- and low-MW poly(CL-LA)-MA, and 1-vinyl-2-pyrrolidone (NVP) (Table S2, Supporting Information). Each formulation also included 1% (w/w) photoinitiator (phenylbis(2,4,6-trimethyl-benzoyl)phosphine oxide (BAPO)), 0.5% (w/w) vitamin E to inhibit premature crosslinking, and 0.1% (w/w) Sudan I dye to control light penetration during printing (Table S2, Supporting Information). To ensure suitable viscosity for DLP, resins were processed at a printing temperature of 75 °C (Figure S6, Supporting Information). Among the 3D-printed dog-bone-shaped elastomers, those obtained from R2 demonstrated favourable mechanical properties, with an average Young's modulus of 2.2 ± 0.2 MPa and the highest elongation at break (≈199%). These values closely resemble those of Shore A 50 (ShA 50) silicone used for the fabrication of our previous prototype (Young's modulus: 1.7 ± 0.03 MPa; elongation at break: ≈180%) (Figure S7, Supporting Information). Therefore, R2 was selected for device fabrication. Further analysis of the 3D-printed R2 specimens revealed their amorphous nature (glass transition temperature (Tg) ≈−36 °C) and the absence of reactive double bonds post-printing, indicating successful photopolymerization compared to the unpolymerized resin (Figures S8 and S9, Supporting Information).

2.3. Mechanical Characterization of 3D-Printed Device and Disintegration in Composting Conditions

The device design was slightly modified from the silicone prototype to enable 3D printing (Figure S10, Supporting Information). Specifically, a thin sacrificial membrane was added at the base of the suction cup to seal the structure during printing and then manually removed post-fabrication with a scalpel (**Figure 2**A; Figure S10, Supporting Information). Additionally, the wall thickness of both the suction cup and the storage compartment was increased to achieve a negative pressure value comparable to that of the original silicone device, while still allowing compressibility (Figure S11, Supporting Information). To ensure a fair comparison, the same design modifications were applied to the silicone version, and both devices were evaluated in terms of force-displacement behavior (Figures 2B; Figure S12, Supporting Information). As shown in Figure 2B, the increased wall thickness resulted in stiffer devices (both the 3D-printed and the silicone versions), requiring greater force compared to the original silicone prototype to achieve compression, generate sufficient negative pressure, and ensure MN exposure. Specifically, a compression force of 30 N resulted in a 2.8-mm displacement in the 3D-printed device, in contrast to the 10 mm displacement achieved by the original silicone version reported in our previous work.[21] Nevertheless, the deformation curve (Figure 2B) indicates that higher displacements, up to 10 mm, can still be achieved by increasing the applied force to 50 N. This force level can be attained during a typical two-handed operation, where compression is applied by the thumbs while stabilization of the device is achieved by the index fingers.[35] Although this operation process is not suitable for self-application on the upper arm, it may be feasible for use on other body regions (e.g., the leg) or enable teachers or parents to perform blood collection in children in non-laboratory settings. Additionally, batch-to-batch variability in polymer synthesis and resin composition led to a higher variability in the force-displacement response of the 3D-printed device compared to its silicone counterpart (Figure 2B).

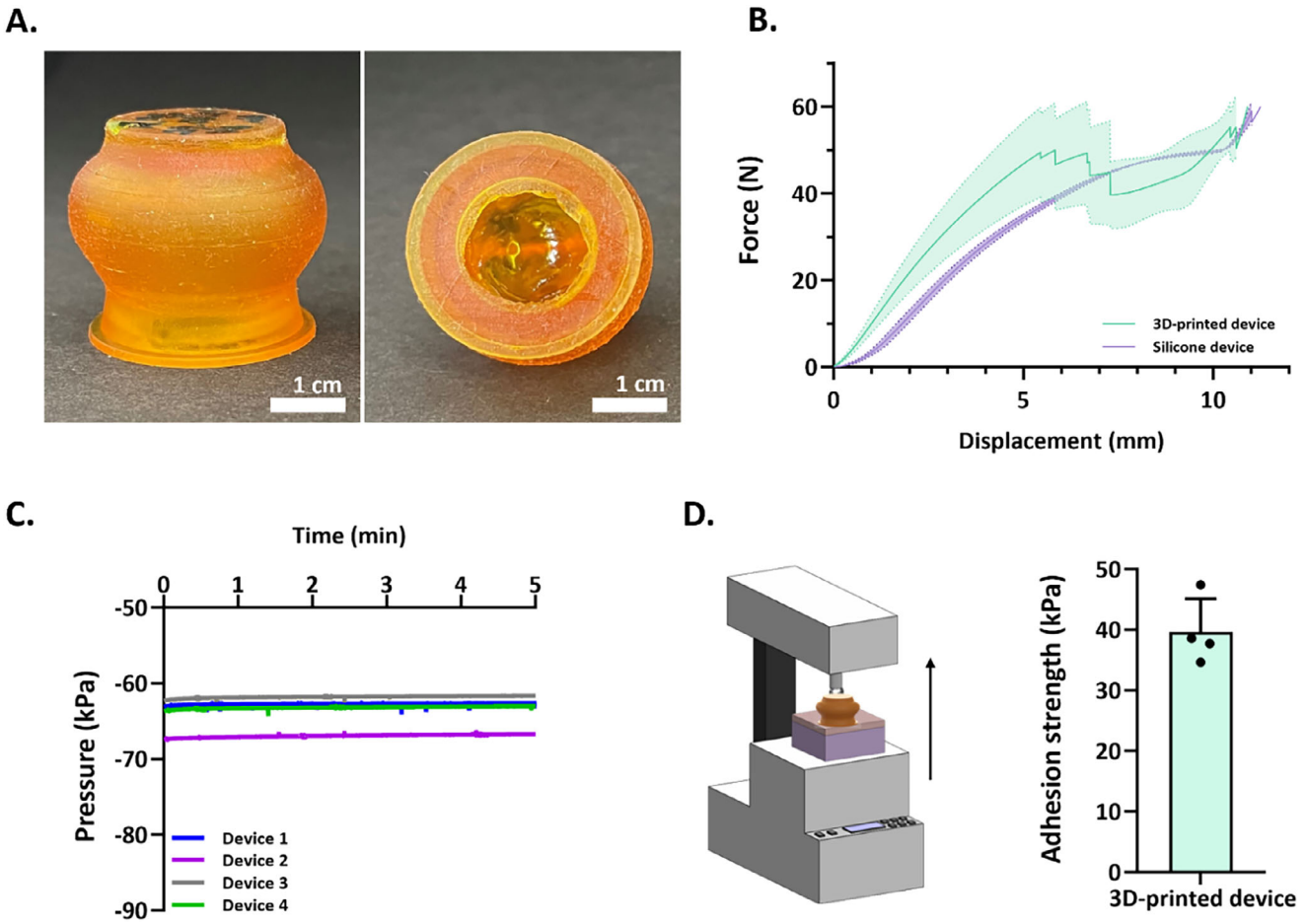

Figure 2. Mechanical characterization of the 3D-printed device. A) Front (left) and bottom (right) views of the 3D-printed device after post-curing and removal of the sacrificial bottom membrane. A schematic representation of the sacrificial membrane is provided in Figure S10A,B (Supporting Information). Scale bar: 1 cm. B) Compression profiles of the 3D-printed device compared to the silicone counterpart with identical geometry (n = 3–9). Data are expressed as mean ± SD. C) Representative negative pressure profiles of four different devices over 5 min, simulating the time of device application for blood collection. Each curve represents one of three replicates. D) Adhesion strength of the 3D-printed device, measured ex vivo by manually compressing the device onto freshly extracted porcine skin cheek and recording the pull-off force at a 0° angle (n = 4). Data are expressed as mean + SD.

To improve ergonomics and enable self-application, alternative degradable polymers and fabrication methods could be explored. While 3D printing with in-house resins at 75 °C allowed rapid prototyping, it limited the MW and range of crosslinkable polymers that could be used. Techniques such as injection molding could enable higher-MW or thermally crosslinkable polymers with greater elasticity, potentially reducing the force required to fully compress the device while maintaining sufficient negative pressure for blood sampling. Additionally, incorporating a one-step actuation mechanism—similar to commercially available self-microsampling devices (e.g., TAP and Tasso)—could facilitate self-application on the upper arm, although this may increase design complexity and production costs.[36]

The negative pressure generated by the 3D-printed device, driven by its elastic self-recovery after compression, was −64 ± 3 kPa (Figures 2C; Figure S13, Supporting Information), slightly lower than that of the original silicone device (−74 ± 8 kPa). In ex vivo experiments using freshly excised porcine cheek skin, this pressure induced an average skin stretching of ≈4.5 mm, slightly lower than the 5.8 mm observed with the previous silicone prototype, probably due to intrinsic variability in porcine tissues (Figure S14, Supporting Information). Nevertheless, by using the previously reported equation (experimentally determined using the Nimble setup (see Histological evaluation of the stretched porcine skin after ex vivo device application)) to correlate negative pressure with skin deformation, it was found that only a small fraction of the total pressure (≈8%) contributed to tissue displacement in the 3D-printed device, similarly to the original silicone device (≈19%).[21] This suggests that the majority of the pressure (≈59 kPa) may still be available for blood sampling, as in the silicone prototype (≈60 kPa). These findings indicate that, despite lower overall pressure and skin stretching, the 3D-printed device may achieve comparable in vivo performance, owing to significantly lower pressure loss for skin stretching.

Thereafter, the adhesive properties of the degradable device were assessed ex vivo on freshly extracted porcine skin by measuring the pull-off force with a texture analyzer (Figures 2D; Figure S15, Supporting Information). The 3D-printed device exhibited a

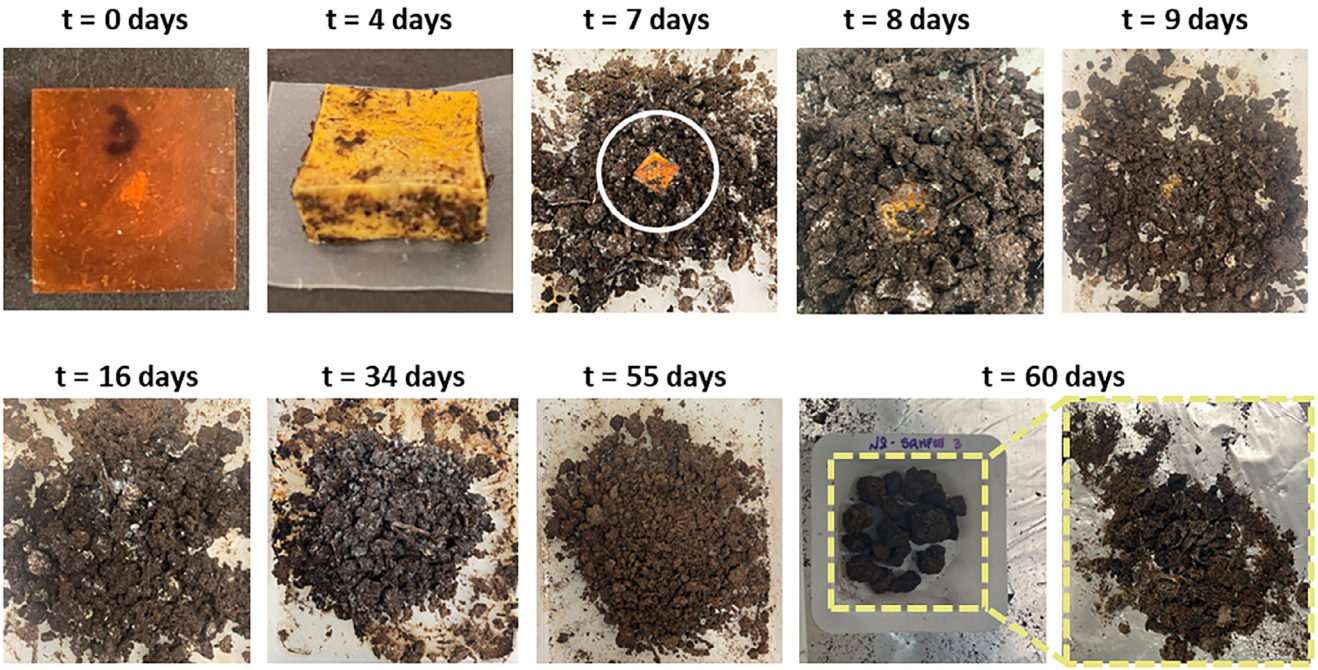

Figure 3. Degradation of poly(CL-LA) in synthetic waste. Representative photographs showing the progressive degradation of a poly(CL-LA) test sample during incubation in synthetic waste at 58 °C over time. Note that the image on the right within the yellow box at the 60-day time point is a magnified view of all the largest compost fragments retained by the sieve at the end of the test, following manual examination and rupture. Images from all tested samples ($n = 6$) are provided in the Supporting Information.

vertical adhesion force of 40 ± 5 kPa, which resembles the results obtained with the original silicone prototype (49.7 ± 2.3 kPa). These adhesion forces align well with the negative pressure measurements (64 vs 74 kPa), further supporting comparable performance between the two devices. Finally, in vitro sampling experiments were performed using a customized Franz cell-type setup. The system featured a ShA 13 silicone layer to replicate the mechanical resistance of human skin, a crosslinked gelatin matrix to simulate tissue porosity, and was filled with freshly extracted oxalate-treated porcine blood. Using this model, the degradable device (without MNs), manually compressed onto the surface, was able to collect 668 ± 291 µL of blood (Figure S16, Supporting Information). These results suggest that, upon efficient skin puncturing, the negative pressure generated by the elastic self-recovery of the material would be sufficient to drive blood flow and enable its collection in the storage compartment of the device. Although this represents a simplified skin model, it is supported by our previous studies, where the same level of negative pressure enabled efficient blood collection in vivo.[21]

Next, to evaluate the degradability of the 3D-printed R2 material, dog-bone-shaped specimens were incubated in phosphate-buffered saline (PBS) at 50 °C, and their dry mass, water uptake, and the pH of the incubation medium were monitored over time (Figure S17, Supporting Information). During the first week, no significant changes were detected. However, from week 2, progressive degradation was observed, characterized by increased swelling, mass loss, and pH drop. By day 36 (end of the test), nearly all samples started to collapse, with an average mass loss of ≈20% (Figure S17A,D,E, Supporting Information). Additionally, the degradability behavior of the 3D-printed material was assessed under simulated composting conditions, in accordance with the International Organization for Standardization (ISO) 20200:2015 guidelines, which evaluate the disintegration of plastic materials. To this end, 3D-printed R2 blocks (15 × 15 × 5.7 mm, ≈1.5 g) were incubated at 58 °C for 60 days in a moist synthetic waste environment, using a specimen-to-waste mass ratio of 1:100. After one week, the specimens showed an average weight loss of ≈11 % (Figure S18, Supporting Information). Subsequently, they softened and developed a sticky, semi-solid consistency, and by day 16, no visible yellowish–orange residues could be identified in the compost material (Figure 3; Figure S19, Supporting Information). Degradation was also accompanied by a slight alkalinization of the synthetic composting mixture (Figure S18, Supporting Information). At the end of the test period (day 60), compost fragments retained by the sieve were collected and manually examined. No traces of the original material were detected (**Figure 3**; Figure S19, Supporting Information).

2.4. Characterization and Degradation of Mg MN Patch

Recently, Mg and its alloys have emerged as promising alternatives to traditional metals, such as stainless steel and titanium, especially in the manufacturing of biodegradable implants. They offer excellent biocompatibility and high mechanical strength while eliminating the need for surgical removal post-implantation.[32,37] Therefore, Mg was selected as the degradable material for fabricating the MN blades, keeping the same blade geometry as in our former work.[21] Indeed, customized Mg MN blades, each consisting of five needles with a length of 2 mm,

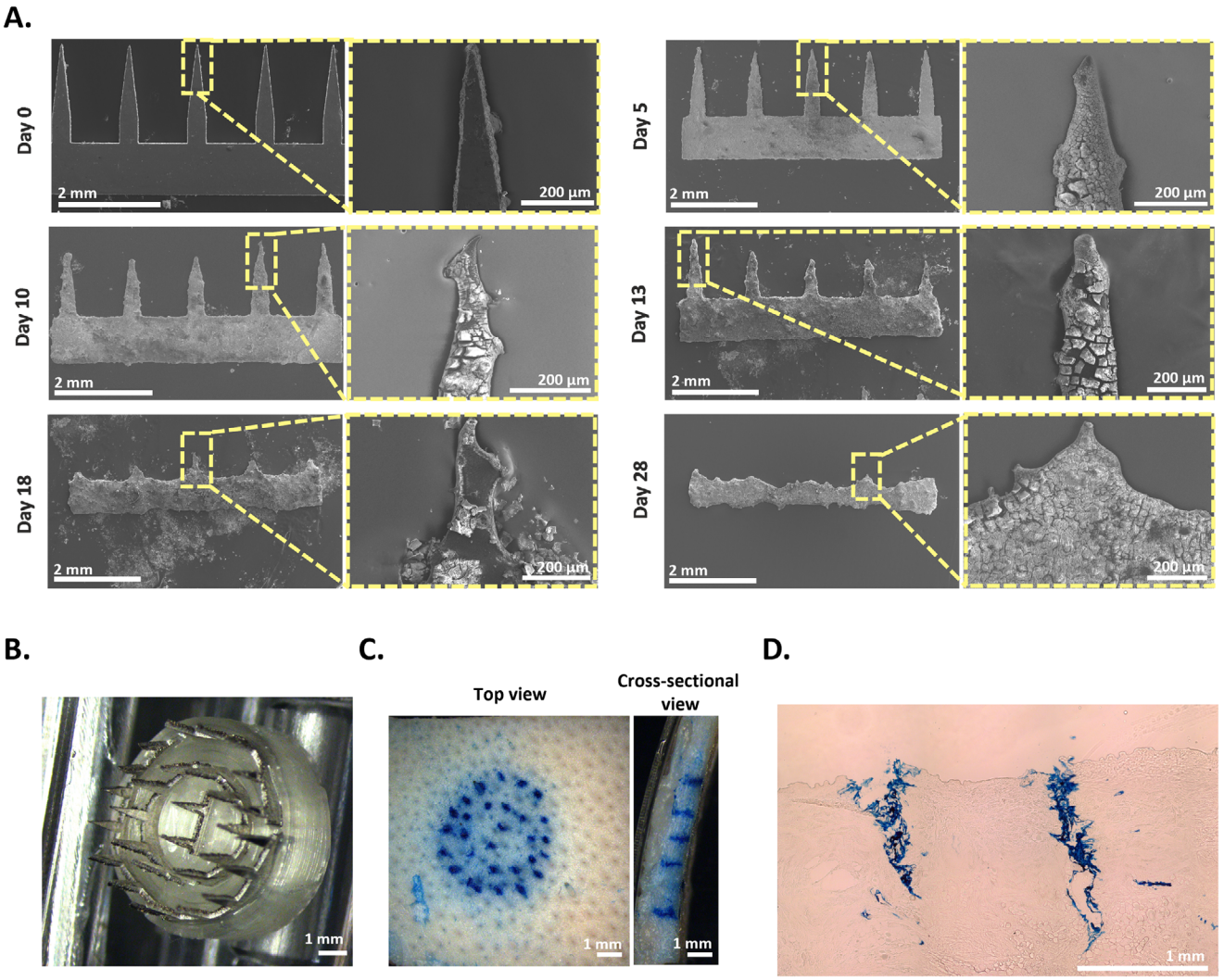

Figure 4. Characterization of degradable Mg MN patch. A) SEM images of Mg blades incubated in PBS (pH 7.4, RT) at different time points, suggesting their rapid degradation. Scale bars: 2 mm and 200 µm. B) Photograph of the final circular Mg MN array composed of 30 MNs selected for the assembly of the degradable device. Scale bar: 1 mm. C) Top view (left) and cross-sectional view (right) of the porcine ear skin following ex vivo puncturing with the dye-coated circular Mg patch. Scale bar: 1 mm. D) Cross-sectional micrograph of porcine ear skin after the ex vivo puncturing experiment with a dye-coated circular Mg MN array, confirming MN penetration into the deep dermal layer. Scale bar: 1 mm.

width of 0.35 mm, and tip angle of ≈13°, were manufactured via nitrogen laser cutting. Four blade thicknesses were evaluated in terms of mechanical strength and efficiency of skin penetration (Figure S20 and Table S3, Supporting Information). Among the blades, those with a thickness of 200 µm were selected, as thicker blades (500 µm) required excessive force to penetrate porcine skin ex vivo, while thinner blades (100 and 150 µm) exhibited bending during insertion (Figure S20, Supporting Information). Thereafter, the degradation behavior of the Mg MNs was evaluated in PBS at room temperature (RT), confirming a near-complete degradation after 40 days of incubation (**Figures** 4A; Figure S21, Supporting Information). To assemble the MN arrays, six blades were glued to 3D-printed PLA basins, forming a circular MN patch with 30 MNs (Figure 4B). The resulting dye-coated patches were tested ex vivo on freshly excised porcine skin, achieving an average penetration depth of ≈1.5 mm, thus confirming that the circular array effectively reached the deeper dermis, where capillaries are located (Figure 4C,D).

2.5. In Vitro Evaluation of Material Hemocompatibility

Hemocompatibility is a critical factor limiting the clinical use of blood-contacting biomaterials, as interactions with these materials can alter blood sample integrity and compromise the accuracy of laboratory results.[38] Erythrocytes, due to their rigidity, are especially prone to rupture under shear stress and osmotic changes.[39] Therefore, to assess the hemocompatibility of the compostable version of the blood microsampling device, a preliminary hemolysis assay was performed on both the 3D-printed part and Mg MN patch. To preserve sample quality, freshly extracted porcine blood was used within 2 h of collection. Blood

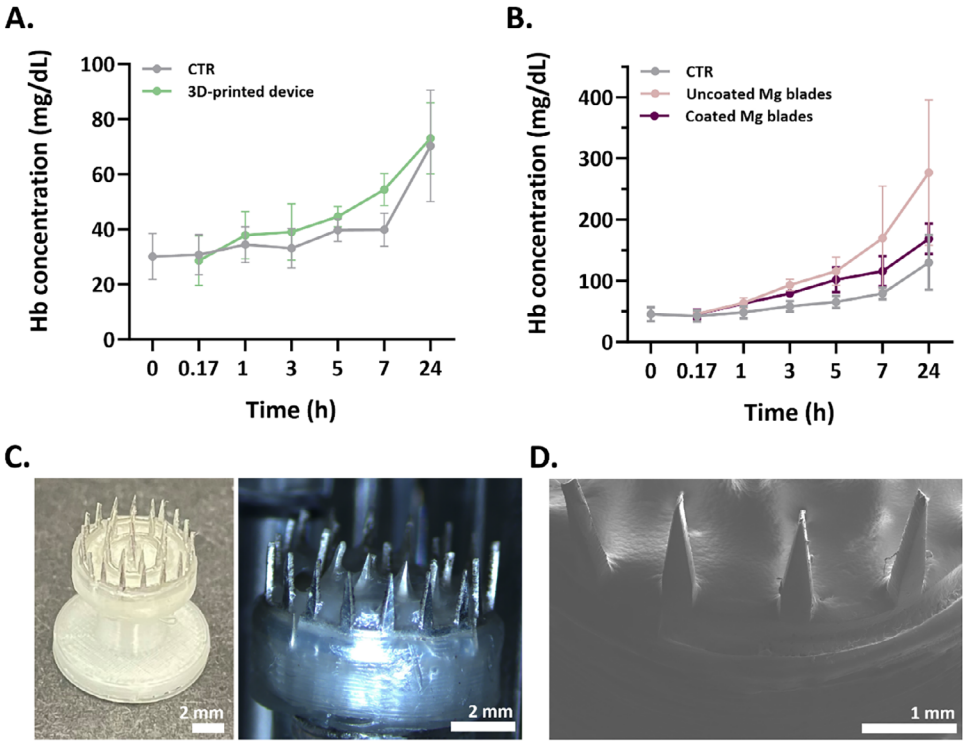

Figure 5. Hemocompatibility assessment of device components. A) Hemoglobin (Hb) concentration in porcine plasma samples collected after centrifugation of whole blood in contact with the 3D-printed device (no blades) at various time points, compared to control (CTR) samples. For the CTR, 1 mL of porcine whole blood was stored in a 2 mL Eppendorf tube. B) Hb concentration in plasma after exposure to coated and uncoated Mg blades, compared to the CTR. Data are presented as mean ± SD ($n = 3$). C) Photographs of the coated Mg MN patch at different magnifications. Scale bar: 2 mm. D) Representative SEM image of the PCL-coated MN patch. Scale bar: 1 mm.

stored in a sealed Eppendorf tube was used as a control. In the case of the 3D-printed reservoir (no blades), hemoglobin (Hb) concentrations in plasma samples slightly increased over time, with no significant differences observed between the compostable device and the control. Notably, after 24 h—an interval sufficient for shipping the sample to nearby laboratories—Hb levels in plasma remained below 100 mg dL^{-1}, and blood pH remained stable (**Figure 5A**; Figure S22, Supporting Information). Although a slight difference in pH was observed at 3 and 5 h, no significant change was recorded at 24 h (Figure S22, Supporting Information). Additionally, the swelling behavior of poly(CL-LA) in contact with blood was evaluated over 24 h, as absorption of blood components by the material could also affect the accuracy of analytical results (Figure S23, Supporting Information). Specifically, no significant changes were observed in the appearance of the material or its swelling after 24 h. Nevertheless, further validation is required to confirm the long-term compatibility of poly(CL-LA) for blood storage and to rule out any alterations in the concentration of specific analytes.

In contrast, Mg blades showed rapid degradation upon immersion in simulated body fluid (SBF), with significant material degradation observed after 24 h, as well as in whole blood (Figure S24, Supporting Information). Furthermore, this degradation was accompanied by a significant increase in hemolysis and blood pH, making the sample unsuitable for analytical purposes (Figure 5B; Figure S25, Supporting Information). Thus, Mg blades were coated with 6 layers of PCL (MW 50,000 g mol^{-1}) (Figure 5C). The coating was homogeneous, with an average thickness of ≈100–135 µm, though thinner at the bottom of the blade (Figure S26, Supporting Information). The PCL coating effectively slowed Mg degradation, reduced hemolysis, and contributed to prolonged pH stability of the stored blood (Figure 5B). Nevertheless, after 3 h of storage, blood samples exposed to the coated MNs also showed elevated hemolysis and pH levels compared to the control, but significantly lower than in samples exposed to uncoated blades. Accordingly, samples in contact with the coated Mg blades maintained acceptable quality for up to 3 h post-collection. It should be noted that this 3 h stability window may not align with logistical realities in LMICs, where reliable storage, refrigeration, and transport infrastructure are limited, and samples may take several days to reach analysis laboratories.[40] In this context, the device's small size, low weight, and robust housing could make it compatible with innovative delivery methods, such as drone-based transport (e.g., Zipline).[41] Additionally, while the polymeric coating of Mg MNs may be a feasible strategy for tuning material properties and preserving both blade integrity and blood sample quality, further optimization remains essential. Specifically, alternative coating techniques, such as spray coating, may offer improved uniformity and performance over the dip-coating method. Additionally, employing different Mg alloys for Mg fabrication, which have been reported to enhance blood stability, could further prolong blood preservation.[42]

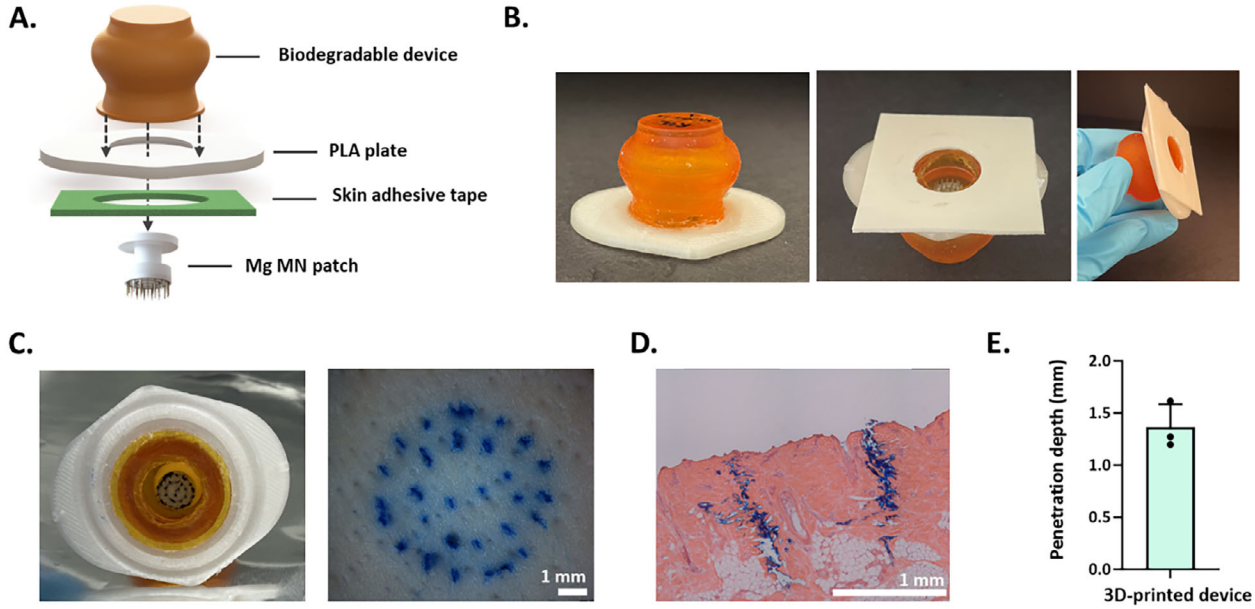

Figure 6. Assembly and ex vivo evaluation of the nearly fully degradable microsampling device. A) Schematic representation of the final device assembly. The prototype integrates a circular Mg MN patch into a 3D-printed, degradable body, which is glued to a PLA base and sealed with a medical-grade adhesive to ensure an airtight seal with the skin. B) Front, top, and side views of the fully assembled degradable device. C) Photographs of the prototype with PCL-coated Mg MN patch (left) and porcine ear skin after prototype application (right). Scale bar: 1 mm. D) H&E-stained section of porcine skin showing successful MN penetration after device application. Scale bar: 1 mm. E) Ex vivo penetration depth of coated-Mg MNs after prototype application. Data are presented as mean + SD ($n = 3$).

2.6. Prototype Assembling and Ex Vivo Testing

To assemble the final prototype, the PLA basin, onto which six Mg blades (30 MNs in total) were embedded, was first coated with 6 layers of PCL (Figure 5C,D). The coated MN patch was then glued in the fluid storage compartment of the device, specifically at the center of its inner top surface. As with the original silicone prototype, the degradable device was equipped with a 3D-printed PLA base plate to facilitate manual compression during application and enable effective MN exposure (**Figure 6**A,B). The resulting device featured a compact design with dimensions comparable to both the previous silicone prototype and existing commercial microsampling systems. To avoid coagulation within the storage compartment, 1.5 mg of potassium ethylenediaminetetraacetic acid (K_2-EDTA) was added. Finally, the prototype was provided with a medical-grade ECG adhesive to ensure a secure seal against the uneven texture of the skin during sampling. Although non-degradable, the use of ECG tape was supported by in vivo experiments performed with the silicone prototype, which confirmed its effectiveness in maintaining an airtight seal on the rough skin surface of piglets. To further reduce waste generation, future strategies could involve degradable double-sided adhesive as well as medical spray adhesives. The latter could be applied directly to the target area, followed by compression of the device against the skin until the adhesive dries and forms an airtight seal, and can subsequently be removed with rubbing alcohol after device detachment. Ex vivo testing of the assembled prototype confirmed successful skin penetration, with an average MN insertion depth of ≈1.4 mm—sufficient to reach the dermal capillary bed and enable efficient blood sampling (Figure 6C–E). Finally, SEM imaging of the PCL-coated MN array following ex vivo application revealed that the PCL coating was largely retained on the patch, with only minimal bending observed at the tips of a few MNs (Figure S27, Supporting Information).

3. Conclusion

In this work, we developed an almost fully degradable blood microsampling prototype fabricated via DLP using a tailored methacrylated poly(CL-LA)-based resin. The device was equipped with a degradable Mg MN patch, manufactured through nitrogen-laser cutting. By optimizing resin formulation and device geometry, we achieved adhesion strength and negative pressure values comparable to those of the previously developed silicone system. The printed material demonstrated rapid disintegration under ISO 20200:2015 simulated composting conditions and gradual degradation in aqueous buffer, confirming its potential as an environmentally sustainable alternative for capillary microsampling. Mg MNs effectively penetrated porcine skin, reaching the deeper dermal layer where capillaries are located, and showed complete degradation in aqueous buffer. To improve stability in whole blood, the MN patch was coated with 6 layers of PCL, which limited premature degradation. Hemocompatibility studies confirmed that both the 3D-printed device and coated Mg MN patch maintained blood sample integrity over short-term storage, with minimal hemolysis and stable pH observed for up to 3 h. Unfortunately, this time period may not consistently align with typical transport times to nearby laboratories. Therefore, further optimization—particularly of the MN coating, selection of Mg alloys, and post-printing washing steps of the device—is necessary before advancing to further testing

(e.g., in vivo blood sampling studies). Additionally, while 3D printing enabled rapid prototyping, efficient screening of different device designs, and decentralized production, it can be replaced by straightforward scale-up through molding processes, making the production of degradable devices feasible even in low-resource settings. This scalability could be achieved by replacing the UV-crosslinkable polyesters synthesized here with degradable, injection-moldable polymers or thermally crosslinkable alternatives.[34] Finally, the optimized degradable prototype would require sterilization (e.g., via gamma irradiation) followed by an investigation of the effects of the sterilization process on the individual components. Overall, this work demonstrates the feasibility of developing fully degradable solutions for capillary blood collection to broader efforts toward sustainable diagnostics. The proposed device holds particular promise for use in LMICs, where conventional medical waste disposal remains a major challenge.

4. Experimental Section

Materials: Pentaerythritol, methacryloyl chloride (97%), triethylamine (Et_3N), (+)-alpha-tocopherol type V (vitamin E), 3,6-dimethyl-1,4-dioxane-2,5-dione (rac-lactide (LA)), tin(II)-2-ethylhexanoate [$Sn(Oct)_2$], ethylene glycol, sodium bicarbonate ($NaHCO_3$), sodium chloride (NaCl), potassium chloride (KCl), dipotassium hydrogen phosphate trihydrate ($K_2HPO_4{\cdot}3H_2O$), magnesium chloride hexahydrate ($MgCl_2{\cdot}6H_2O$), calcium chloride ($CaCl_2$), sodium sulfate (Na_2SO_4), tris(hydroxymethyl)aminomethane ($(CH_2OH)_3CNH_2$), NVP (≥99%), BAPO, 1-(phenyldiazenyl)naphthalen-2-ol (Sudan I), tetrahydrofuran (>99.5%, high-performance liquid chromatography (HPLC) grade) (THF), 2-propanol (isopropanol) (≥99.8%, for cleaning), acetone (≥99.8%, for cleaning), 2-methylbutane, methanol-free paraformaldehyde (PFA), gelatin from porcine skin type A, dichloromethane (CH_2Cl_2), sodium sulfate anhydrous (Na_2SO_4, ≥99.0%), hydroxyethyl cellulose (medium viscosity), and PBS pH 7.4 tablets were purchased from Sigma–Aldrich. Chloroform-d ($CDCl_3$) was obtained from Apollo Scientific. Hydrochloric acid (37%) (HCl) and urea were purchased from VWR. ε-caprolactone (CL) (>99%) was obtained from Tokyo Chemical Industry. Modified Eagle's medium (DMEM) Nutrition Mixture (with glutamine and without phenol red) (DMEM/F12) and antibiotic-antimycotic 100X (10 000 U of penicillin, 10 mg of streptomycin, and 25 µg of amphotericin B per mL) were purchased from Thermo Fisher Scientific. ProLong Diamond Antifade Mountant was purchased from Invitrogen. K_2-EDTA extra pure was obtained from Fisher Chemicals. Smooth-Sil 950 platinum cure silicone with ShA 50 was purchased from Smooth-On. RTV2 platinum silicone with ShA hardness of 13 was purchased from Silikonfabrik. Optimal cutting medium (OCT) was purchased from Leica Microsystems. Magnesium foils ≈500, 200, 150, and 100 µm were obtained from ESPI Metals. Customized Mg blades were manufactured using nitrogen laser cutting at ETH Zurich, in the mechanical workshop of the Physics Department. SPECTRUM PLA tough natural filament, 1.75 mm was purchased from 3D printerstore. Hb Assay Kit (Colorimetric) was purchased from Abcam. Whole porcine blood treated with oxalate as an anticoagulant was obtained from the local slaughterhouse (Schlachtbetrieb Zürich AG). ECG adhesive tape was kindly provided by Adhex. Saccharose (granulated sugar) and corn starch (Maizena) were purchased from Coop. Sawdust (from beech wood, 0.1–1 mm corn size) was obtained from MycoGenetics Pilz-Shop. Rabbit feed (MultiFit, Alfalfa) was bought from Fressnapf (MultiFit Tiernahrung). Cornseed oil was obtained from Roth AG. Ripe, high-quality compost was kindly provided by Caìscio Compost Sagl. All materials were used as received.

Methods—Polymer Synthesis: High- and low-MW poly(CL-LA) were synthesized via ROP of LA and CL, using pentaerythritol (4-arm initiator) or ethylene glycol (2-arm initiator), respectively, with $Sn(Oct)_2$ as a catalyst (Figure S1, Supporting Information). The MW of the polymers was controlled by adjusting the molar feed ratio of monomers to initiators. Subsequently, poly(CL-LA) was functionalized with methacryloyl chloride in CH_2Cl_2, using Et_3N as a base.

Specifically, for the synthesis of low-MW poly(CL-LA) (2-arm, MW = 500 g mol^{-1}, CL/LA molar ratio of 5/5), ethylene glycol (2 g, 32.2 mmol), CL (7 mL, 62.8 mmol), LA (9.06 g, 62.8 mmol), and $Sn(Oct)_2$ (104 µL, 0.322 mmol) were added to a Schlenk flask. The flask was subjected to three cycles of vacuum and argon purging to eliminate residual water and oxygen. Thereafter, it was placed in an oil bath at 140 °C and stirred overnight to allow polymerization. The crude product was dissolved in 80 mL of CH_2Cl_2 and transferred into a round-bottom flask. Subsequently, 12 mL of Et_3N was added, and the flask was placed in an ice bath under a nitrogen atmosphere. 7 mL of methacryloyl chloride, pre-diluted in 20 mL of CH_2Cl_2, was then slowly added dropwise to the reaction mixture over 30 min. The reaction was allowed to proceed overnight in the dark under nitrogen. Subsequently, the product (low-MW poly(CL-LA)-MA) was washed sequentially with 1 M HCl, saturated $NaHCO_3$ solution, and brine to remove residual reagents. The organic phase was then dried over anhydrous Na_2SO_4, and 5 drops of vitamin E were added to the supernatant to prevent premature cross-linking. Finally, the solvent was removed under vacuum using a rotary evaporator, and the transparent polymer was dried under high vacuum for 24 h (≈95% yield).

The same procedure was used to synthesize high-MW poly(CL-LA) (4-arm, MW = 15,000 g mol^{-1}, CL/LA molar ratio of 7/3). In this case, pentaerythritol (0.38 g, 2.8 mmol), CL (26.4 mL, 238 mmol), LA (14.52 g, 100.8 mmol), and $Sn(Oct)_2$ (9 µL, 0.0278 mmol) were added to a Schlenk flask. For the methacrylation step, 2.5 mL (16.3 mmol) of Et_3N was added to the product previously dissolved in 160 mL of CH_2Cl_2. Thereafter, 2 mL (15 mmol) of methacryloyl chloride, pre-diluted in 5 mL of CH_2Cl_2, was then added dropwise to the reaction mixture over 30 min. The product (high-MW poly(CL-LA)-MA) was subsequently washed with 1 M HCl, saturated $NaHCO_3$ solution, and brine, following the same procedure as for the low-MW poly(CL-LA)-MA. The resulting transparent to yellowish viscous polymer was dried under high vacuum for 24 h (≈90% yield).

Methods—Polymer Characterization: ^1H NMR spectra of crude and methacrylate poly(CL-LA)s were recorded on a Bruker AV400 spectrometer (Bruker Corporation) at 400 Hz using $CDCl_3$ as a solvent. Following polymerization, the % conversions of LA and CL were calculated using Equations (1) and (2):

$$LA_{\%} = \frac{A_{5.2\ ppm}}{A_{5.2\ ppm} + A_{5.4\ ppm}} \times 100 \quad (1)$$

$$CL_{\%} = \frac{A_{2.3\ ppm}}{A_{2.3\ ppm} + A_{2.7\ ppm}} \times 100 \quad (2)$$

where A represents the area under the corresponding peak in the spectrum.

Gel permeation chromatography (GPC) was performed on an Agilent 1260 Infinity II system equipped with two Shodex LF-804 columns (styrene divinylbenzene copolymer, Resonac) and a differential refractive index detector (Optilab). Samples were dissolved in THF, filtered through a 0.22-µm syringe filter (Chromafil, Macherey–Nagel), and eluted with THF as a mobile phase at a flow rate of 1 mL min^{-1}. Number-average molecular weight (M_n GPC) and dispersity (Đ), determined via GPC, were calculated relative to a polystyrene standard curve with MWs of 580, 2970, 4490, 10 680, 30 230, 170 800, and 1 820 000 g mol^{-1}. Differential scanning calorimetry (DSC) was performed using a TA Q200 DSC (TA Instruments-Waters LLC). Approximately 10–15 mg of each sample were placed in Tzero hermetic pans (TA Instruments–Waters LLC) and subjected to a heat–cool–heat cycle under a constant nitrogen flow of 50 mL min^{-1}. The temperature range was set from −80 to 170 °C for low-MW poly(CL-LA)-MA, and from −80 to 250 °C for high-MW poly(CL-LA)-MA, as well as for the 3D-printed samples. A heating and cooling rate of 10 °C min^{-1} was used. Data were analyzed using TA Instruments

Universal Analysis 2000 software (version 5.5.3). Fourier-transform infrared (FTIR) spectroscopy was conducted in transmission mode using a Perkin–Elmer Spectrum 2 (Perkin–Elmer Inc.) spectrometer, over a spectral range of 450–4000 cm^{-1}. Viscosity measurements of R2 resins were performed using a HAAKE RheoStress 600 rotational rheometer (Thermo Electron Corporation) equipped with a cone-plate geometry (35 mm/2°). Viscosity curves were determined under the following conditions: I) at a constant shear rate of 10 s^{-1} over a temperature range of 25–90 °C with a heating rate of 0.05 °C s^{-1} (Figure S6A, Supporting Information); II) over time at a constant temperature of 75 °C and shear rate of 10 s^{-1} (Figure S6B, Supporting Information); and III) at a fixed temperature of 75 °C (representing the printing temperature) and a shear rate ranging from 0.01 to 1000 s^{-1} (Figure S6C, Supporting Information). Data were analyzed using RheoWin Data Manager (Thermo Electron Corporation).

Methods—Resin Preparation and DLP 3D Printing: Resins were prepared by dissolving BAPO (photoinitiator, 1.0% (w/w)) and Sudan I (blue light-absorbing dye used to reduce curing depth, 0.1% (w/w)) in NVP (reactive diluent, 18–20% (w/w)). Subsequently, high- and low-MW poly(CL-LA)-MA polymers (80–82% (w/w)) and vitamin E (radical inhibitor to prevent premature crosslinking, 0.5% (w/w)) were added to the mixture (Table S2, Supporting Information). The resins were first mixed manually with a spatula and then homogeneously mixed by vortexing. 3D printing was carried out using a commercial Asiga MAX X DLP printer (Asiga) with a 27-µm resolution, equipped with a 405 nm light source, a customized resin tray, and a heated printing head.[29] The printing was performed at 75 °C with a standard layer exposure time of 8.3 s, and an initial exposure time of 30 s. The degradable device and dog-bone-shaped specimens were designed in SolidWorks (Dassault Systèmes SE). Following 3D printing, the sacrificial membrane at the base of each printed device was carefully removed with a scalpel (Figure S10A,B, Supporting Information). Thereafter, 3D-printed dog-bone-shaped tensile test specimens were sonicated in a 90:10 (v/v) 2-propanol:acetone mixture for 1 min at 60 °C using a sonicator bath (Ultrasonic cleaner, Labmaterial or Bandelin Sonorex, Bandelin electronic). 3D-printed devices were cleaned using the same procedure for 5 min, with the washing step repeated three times. Finally, all printed objects were post-cured in a UV chamber (CL-1000 Ultraviolet Crosslinker, UVP) for 20 min and stored under vacuum to prevent moisture absorption.

Methods—Design of Molds and Stamps for the Fabrication of the Silicone Device: For the fabrication of the silicone device, the design created in SolidWorks was converted into a negative casting mold and stamp, which were then multiplied (2 × 2), enabling the fabrication of 4 devices simultaneously (Figure S12, Supporting Information). The molds were exported as.STEP files and provided with 4 threaded holes ($d = 4$ mm) using Fusion Autodesk 360. Subsequently, both molds and stamps were exported as. STL files and 3D printed via LCD printing (Jenny Light 1+) with a Value Line UV/DLP Tough (ABS-like) clear resin with a layer thickness of 0.1 mm. After printing, both parts were washed twice with 2-propanol in a sonicator bath (Ultrasonic cleaner, Labmaterial or Bandelin Sonorex, Bandelin electronic) at 40 °C for ≈30 min, followed by a quick rinse with acetone. They were then UV-cured for several hours (CL-1000 Ultraviolet Crosslinker, UVP). Before silicone casting, molds and stamps were exposed to sunlight for ≈10 days to eliminate any residual radicals from the printing process, which could otherwise interfere with the silicone's hardening.

Methods—Tensile Test: Tensile tests were conducted on dog-bone specimens (ASTM 638 type IV) with a gauge length of 12 mm, at a rate of 1 mm min^{-1} using a TA.3DXTplus texture analyzer (Stable Micro Systems) equipped with a 50 N load cell. Tensile tests were performed on dog-bone-shaped specimens fabricated via DLP, as described in resin preparation and DLP 3D printing. For ShA 50 silicone, specimens were prepared by cast-molding using a liquid crystal display (LCD) 3D-printed mold and stamp (Jenny Light 1+). Specifically, poly(dimethylsiloxane) (PDMS) base and platinum curing agent (Smooth-Sil 950) were mixed at a 10:1 (w/w) ratio and degassed under vacuum for 10 min. The mixture was then poured into the mold and vacuum-degassed for an additional 5 min. Subsequently, the stamp was inserted and the resulting assembly tightened in a custom-made, 3D-printed holder (Pro 2, Raise 3D Technologies, Inc.) made of PLA (Spectrum filament PLA tough natural, 1.75 mm) with 4 bolts and nuts to ensure uniform pressure during the overnight PDMS hardening. Afterward, the stamp was removed, and any excess material was trimmed away. Young's modulus was calculated as the slope of the initial part of the stress–strain curve from 3% to 8.6% strain. Three strips of each material were tested ($n = 3$).

Methods—ShA 50 Silicone Device Fabrication Via Cast-Molding: To fabricate the silicone devices, the ShA 50 PDMS base and curing agent were mixed at a 10:1 ratio (w/w). The resulting pre-polymer mixture was degassed under vacuum for 10 min. Subsequently, the mixture was poured into the molds and subjected to an additional 5–10 min of vacuum degassing (Figure S12A, Supporting Information). Following this, the stamps were inserted, and the merged molding plates were tightly clamped to ensure uniform pressure application during the PDMS hardening (Figure S12B, Supporting Information). The process was performed on two molds simultaneously. After an overnight hardening at RT, the stamps were removed, and any excess material was trimmed away (Figure S12C, Supporting Information). The two cleaned molds were then coated with a thin layer of freshly prepared and degassed PDMS pre-polymer (Figure S12D, Supporting Information) and merged. The combined molds were secured in a custom-made, 3D-printed PLA holder (as described in tensile test) using four bolts and nuts and allowed to harden overnight. Finally, the molds were opened, the devices were demolded, and any excess material was removed to obtain the final silicone device (Figure S12E,F, Supporting Information).

Methods—Force-Displacement Measurements: To evaluate device displacement under compression, a TA.3DXTplus texture analyzer equipped with a 50 N load cell was used. A custom-designed, 3D-printed platform, created using SolidWorks and fabricated using an LCD printer (Jenny Light 1+) and Value Line UV/DLP Tough (ABS-like) clear resin, was used as a compression surface (Figure S11, Supporting Information). After printing, the platform was washed twice in a sonicator bath (Ultrasonic cleaner, Labmaterial or Bandelin Sonorex, Bandelin electronic) using 2-propanol for 5 min, followed by UV curing (CL-1000 Ultraviolet Crosslinker). Thereafter, a 2-mm diameter hole was drilled in the platform to facilitate air removal from the device during compression testing. After calibration, the device was placed on the platform's surface and compressed at a rate of 1 mm s^{-1} until a force of 60 N was reached. During the experiment, force-displacement curves were recorded, and the photographs of the device's displacement under a 60 N compression force were taken. Measurements were performed in at least three independent experiments ($n = 3$–9).

Methods—Negative Pressure Measurements: To determine the negative pressure generated by device compression, a custom-built setup was developed.[21] The setup included a 3D-printed platform designed using SolidWorks and fabricated using an LCD printer (Jenny Light 1+) and a Value Line UV/DLP Tough (ABS-like) clear resin. Following cleaning and post-curing (force-displacement measurements), a 4-mm thick silicone layer (ShA 13) was placed on top of the platform, and an Adafruit MPRLS ported pressure sensor breakout (0 to 25 PSI) (Ported Pressure Sensor Breakout, Adafruit Industries) connected to a Raspberry Pi microcontroller (Raspberry Pi 4 Computer, Model B 4GB RAM, Raspberry Pi Foundation) was affixed to the bottom of the setup. A small hole was drilled at the center of the assembly to enable a tubing connection between the sensor and the silicone layer. To measure negative pressure, 3D-printed devices were manually compressed against the silicone surface of the setup, and pressure changes were recorded for up to 5 min. Standard atmosferic pressure (101.325 kPa) was used to calculate the negative pressure of the 3D-printed devices. Minor vacuum leakage was observed during the test, likely due to limitations of the platform. Each measurement was conducted in four independent experiments ($n = 4$).

Methods—Ex Vivo Skin Stretching After Application of the Degradable Device: Ex vivo skin stretching experiments were performed using freshly excised porcine cheek skin obtained from 5- to 6-month-old pigs (100–120 kg), sourced from a local slaughterhouse (Schlachtbetrieb

Zürich AG). Immediately after collection, the skin was immersed in DMEM/F12 medium supplemented with 1% (v/v) antibiotic-antimycotic 100X. All experiments were conducted within 2 h of tissue collection to preserve tissue integrity. The tissue sample was then cut into a 3 × 3 cm piece, onto which the printed device was manually compressed. After 5 min application, the porcine skin with the applied device was snap-frozen by immersion in a nitrogen-cooled isopentane (2-methylbutane) bath for a few min. Following freezing, the device was removed, and the skin sample was embedded in OCT. The embedded tissue was stored at –20 °C for 24 h before being transferred to –80 °C. Transversal sections of 20 µm thickness were prepared using a cryostat (CryoStar NX50, Thermo Fisher Scientific) at –18 °C. Sections were mounted on microscope slides (Thermo Fisher Scientific) and kept at –80 °C until further analysis.

Methods—Histological Evaluation of the Stretched Porcine Skin After Ex Vivo Device Application: Microscope slides (prepared as described in ex vivo skin stretching after application of the degradable device) were thawed at RT for 30 min. The tissue sections were then fixed in a 4% (w/v) methanol-free PFA solution in PBS for 10 min, followed by a 1-min wash in PBS and two rinses with distilled water. To evaluate tissue morphology, the fixed sections were stained with H&E using an automated stainer at the ScopeM facility (ETH Zürich). Briefly, slides were stained twice with Mayer's hematoxylin (Medite AG) for 1.5 min, washed under a gentle stream of tap water, and immersed for 1 min in an HCl-EtOH bluing solution (700 mL absolute EtOH + 299 mL distilled water + 1 mL 37% HCl). After bluing, the slides were rinsed again with tap water before proceeding to the 1.5-min Eosin Y (Chroma–Gesellschaft) staining step. Following this, the sections were then dehydrated and cleared by subsequent immersions in solutions with an increased EtOH concentration (2x 95% EtOH, 2x 100% EtOH) and xylene (Merck KGaA) (2x), respectively. Finally, they were mounted with ProLong Diamond Antifade Mountant (Invitrogen) and covered with a coverslip. Cross-sectional images were recorded using the Leica DMI 6000 B microscope and light source (EL6000 mercury metal halide bulb, Leica Microsystems) with adaptive focus control at a magnification of ×10 (HC PL FLUOTAR L 20×, with correction collar, numerical aperture: 0.4, dry, Leica Microsystems) using LAS X Software (Leica Microsystems) in the tile scan mode (manual and automatic focusing; range, 60 µm) and were merged afterward. Images were detected by a monochrome D FC365FX digital camera (12 bits, 1 × 1 BIN, Leica Microsystems). To quantify the pressure responsible for skin stretching within the device, displacement values (in mm) were input into Equation (3):

$$y = 0.0583\ e^{0.967x} \tag{3}$$

where x is the skin displacement (mm, measured directly in LAS X) and y is the corresponding pressure (kPa). This relationship was experimentally derived using the nimble setup described in the previous work.[21]

Methods—Adhesion Test: Adhesion tests were performed on freshly excised porcine cheek skin, processed as described in ex vivo skin stretching after application of the degradable device. Within 2 h of excision, excess fat and muscle tissue were trimmed from the sample to achieve a uniform thickness of ≈1.5 cm. The skin was then cut into cubes, gently shaved, and glued to a 4 × 4 cm 3D-printed platform, designed in SolidWorks and fabricated via DLP printing (Asiga Max X, 27 µm) using a commercial resin (Asiga Plasclear). Thereafter, the adhesive properties of the 3D-printed devices were evaluated by measuring the pull-off force using a Texture Analyzer equipped with a 50-N load cell (TA.XTplus Texture Analyzer). For the test, a needle was inserted into the device's knob to allow the attachment of a cotton thread connecting the device to the upper pulling clamp of the instrument (Figure S15, Supporting Information). The platform–skin assembly was mounted horizontally (0° platform) on the lower clamp of the testing instrument. To ensure proper sealing between the device and the tissue surface, two drops of a 2% (w/v) hydroxyethyl cellulose solution in distilled water were applied to the skin. The printed device was pulled vertically at a constant rate of 5 mm s^{-1} until detachment. Force-distance curves were recorded using Exponent software (Stable Micro Systems). Vertical adhesion forces (in kPa) were calculated by dividing the maximum force recorded before device detachment by the device's bottom contact area (determined individually for each device to account for variations from the removal of the sacrificial membrane). Measurements were performed in triplicate for each of the four tested devices ($n = 4$).

Methods—In Vitro Sampling: The sampling performance of the printed device was evaluated in vitro using freshly collected porcine whole blood (Schlachtbetrieb Zürich AG) treated with sodium oxalate as anticoagulant. To perform the experiment, a custom Franz-cell was designed in Solidworks and fabricated using an LCD 3D printer (Jenny Light 1+) with a Value Line UV/DLP Tough (ABS-like) clear resin. A highly porous gelatin matrix was placed inside the printed cell to better simulate the in vivo tissue porosity. To replicate skin-like properties and ensure effective device adhesion, a plastic petri dish topped with a 4-mm-thick layer of soft silicone (ShA 13) was glued to the top of the cell. A small hole (d ≈0.5 mm) was drilled through the silicone-petri dish assembly to allow blood sampling. The cell was filled with porcine whole blood, and its lateral arm was sealed with parafilm. Prior to application, a medical-grade adhesive spray (Ulrich medical adhesive B) was applied to the bottom of the device. The device was then manually pressed onto the setup and held in place for a few seconds to allow the adhesive to dry. Once adhesion was achieved, the fingers were removed, and the device was left in place for 5 min. At the end of the experiment, the setup was slightly tilted before detaching the device to prevent blood backflow. The extracted fluid volume was then measured using a 100-µL pipette. A photograph of the complete in vitro fluid extraction setup is shown in Figure S16C (Supporting Information).

The gelatin matrix used to fill the cavity of the custom Franz-cell was prepared by dissolving 4 g of gelatin in 100 mL of distilled water (final concentration 4% w/v) at 50 °C under magnetic stirring. To chemically cross-link the gelatin, 0.5% (v/v) of a 25% (w/v) aqueous glutaraldehyde solution was added. The resulting hydrogel was then frozen at –20 °C overnight to induce cryogelation, and subsequently freeze-dried to obtain a highly porous structure.

Methods—Degradation of 3D-Printed Dog-Bone Specimens in Aqueous Buffers: 3D-printed dog-bone specimens of poly(CL-LA)-MA were immersed in 50 mL of PBS (pH 7.4) at 50 °C, in 50-mL Falcon tubes. The buffer solution was replaced at each sampling time point over a 5-week period. At each time point, samples were removed, rinsed with distilled water, gently wiped, and dried under vacuum for 5 h. Sample weights were recorded before (wt_{wet}) and after (wt_{dry}) the drying step. The water uptake (%) and remaining mass (%) were calculated using Equations (4) and (5), respectively:

$$Water\ uptake\ (\%) = \frac{wt_{wet} - wt_{dry}}{wt_{dry}}\ x\ 100 \tag{4}$$

$$Weight\ (\%) = \frac{wt_{dry}}{wt_{t=0}}\ x\ 100 \tag{5}$$

where $wt_{t=0}$ is the initial mass of the 3D-printed strips.

Additionally, the pH of the degradation medium was recorded at each time point using a Mettler Toledo pH electrode connected to an Orion Dual Star pH/ISE Meter (Thermo Fisher Scientific). Samples were imaged before and after vacuum drying using an optical microscope (Leica MZ6) equipped with Flexcam C3 camera for real-color imaging (Leica Microsystems). All degradation experiments were conducted using five 3D-printed specimens ($n = 5$).

Methods—Device's Disintegration in Synthetic Waste: The compostability of 3D-printed poly(CL-LA)-MA was evaluated in accordance with ISO 20200:2015 guidelines. Specifically, the solid waste mixture was prepared by combining 40% (w/w) sawdust, 30% (w/w) alfalfa-based rabbit feed, 10% (w/w) ripe compost, 10% (w/w) corn starch, 5% (w/w) saccharose, 4% (w/w) cornseed oil, and 1% (w/w) urea. Distilled H_2O was added to achieve a total water content of 55% (w/w). Thereafter, 150 g of wet solid waste were placed in a sealed 33 × 19 × 11 cm poly(propylene) box (Rotho). A 5-mm diameter hole was drilled on each of the two 20 cm-wide sides, ≈6.5 cm above the bottom of the box.

For the preparation of the test material, blocks (15 × 15 × 5.7 mm) composed of R2 resin mixture were 3D printed as described in resin preparation and DLP 3D printing. Notably, the specimen thickness of 5.7 mm was specifically chosen because it corresponds to the thickest wall of the degradable device requiring degradation assessment. After vacuum drying at 40 °C to a constant mass (average specimen weight = 1.47 g; specimen-to-wet synthetic material mass ratio ≈0.98% (w/w)) the specimens were dipped in distilled water for a few seconds and placed in the composting boxes. The disintegration test was performed at 58 °C in an air-circulation oven. At specific time points, the boxes were weighed, the pH of the synthetic composting mixture was measured (Tolesum 3-in-1 Digital Soil Meter with Thermometer/Soil Moisture/pH), and photographs of the specimens were taken. The oven temperature was simultaneously recorded using a TM26 temperature indicator (Extech Instruments). Afterward, fresh water was added to each box to restore the initial wet waste mass (to 100% until day 28 and to 80% from 30 to 60 days), and the composting material was mixed as needed, following ISO 20200:2015 guidelines. On day 7, specimens were retrieved from the soil matrix, gently rinsed with water to remove adhering soil without causing mechanical damage, and dried under vacuum at 40 ± 2 °C to constant weight (≈24 h) before being returned to the composting reactors. As the specimens subsequently transitioned into a sticky, semi-solid state from which the soil could not be removed without compromising sample integrity, weight-loss measurements could not be carried out at later time points. On day 60, the composting matter-specimen mixtures were dried in their boxes at 58 °C with the lids removed until a constant mass was achieved. Clumps were carefully broken apart to avoid damaging any residual sample. The dried mixtures were then sequentially sieved using 10- and 5-mm sieves (Siebmeister 5000, Sterico), followed by a 2-mm sieve (de Buyer). The residual material that did not pass through the sieves was visually inspected, vacuum-dried at 40 °C (KVTS 11) to a constant mass, and then further examined to identify any remaining sample residue. Measurements were performed on six specimens ($n = 6$).

Methods—Mg Blade Fabrication and Ex Vivo Assessment of MN Penetration Force: Mg blades, each featuring 5 MNs and designed in SolidWorks, were fabricated via nitrogen-laser cutting at the mechanical workshop of the Physics Department, ETH Zürich. Specifically, Mg sheets of four different thicknesses, 100, 150, 200, and 500 µm, were used for blade manufacturing (Table S3, Supporting Information). Following laser cutting, the blades were stored under vacuum in a desiccator to minimize exposure to air and prevent oxidation. To assess the mechanical properties of the blades, four out of the five MNs on each blade were carefully removed, leaving only the central MN for testing. The resulting MN was then dipped in a tissue dye solution (Tissue Marking Dye, blue, Diapath) and allowed to dry for 2 h. Thereafter, it was glued to the central channel of a circular basin, which was designed in SolidWorks and 3D printed via FDM (Pro 2, Raise 3D Technologies, Inc.) using PLA (SPECTRUM Filament PLA tough natural, 1.75 mm). The basin featured an 8.4-mm diameter and an overall height of 3 mm, with a central channel (inner d ≈2 mm) to accommodate the MN. Penetration force testing was performed with a texture analyzer (TA.XT plus Texture Analyser, 50 N load cell). Indeed, the basin was attached to the cylindrical compression probe of the instrument using a double-sided tape, placing the MN tip downward. Freshly excised porcine ear skin (prepared as described in ex vivo skin stretching after application of the degradable device for the porcine cheek) was used as the penetration substrate, glued to a 4 × 4 cm 3D-printed platform (as reported in adhesion Test), and mounted on the lower clamp of the instrument. The test was performed at a constant speed of 1 mm s^{-1}. Force-displacement curves were recorded starting from the initial contact between the sensor and the MN tip until a fixed displacement of 2 mm was reached. At the end of the test, cross-sectional incisions were made in the porcine skin to confirm the penetration of the MNs. The penetration force was defined as the peak value on the force–displacement curve before the first noticeable drop, representing skin puncture. Measurements were performed in triplicate for each Mg MN ($n = 3$).

Methods—Degradation of Mg Blades in PBS and Simulated Body Fluid (SBF): Mg blades (200 µm thickness) were immersed in either 50 mL of PBS (pH 7.4) or 15 mL of SBF (pH 7.3) at RT, in closed Falcon tubes. The SBF was prepared according to the method described by Kokubo et al.[43] Briefly, 7.996 g of NaCl, 0.350 g of $NaHCO_3$, 0.224 g of KCl, 0.228 g of $K_2HPO_4{\cdot}3H_2O$, 0.305 g of $MgCl_2{\cdot}6H_2O$, 0.278 g of $CaCl_2$, 0.071 g of Na_2SO_4, 6.057 g of $(CH_2OH)_3CNH_2$, and 40 mL of HCl were dissolved in 1 L of distilled water at 37 °C and adjusted to a final pH of 7.4. Regarding the degradation study, the medium was changed at each sampling time point throughout the study. At each time point, samples were removed, gently wiped, dried under vacuum for 5 h, and their weights recorded (wt_{dry}). The sample remaining mass (%) was calculated using Equation (5), as described in degradation of 3D-printed dog-bone specimens in aqueous buffers, where $wt_{t=0}$ is the initial mass of the Mg blade. Additionally, the pH of the degradation medium was recorded at each time point using a Mettler Toledo pH electrode connected to an Orion Dual Star pH/ISE Meter. Samples were imaged after vacuum drying at different time points via scanning electron microscopy (SEM) (SEM analysis). Degradation experiments were conducted on five Mg blades ($n = 5$).

Methods—FDM Fabrication of PLA MN Holder and Adapter: Both PLA adapter and MN holder were designed in SolidWorks and 3D printed via FDM (Pro 2) with commercial PLA (SPECTRUM Filament PLA tough natural, 1.75 mm). The adapter had the same dimensions as reported in the previous work, with a y-height of 40.6 mm and an x-height of 48.8 mm. It also featured a central hole (d = 20.5 mm) designed to fit the bottom rim of the printed device.[21] The circular MN holder had a diameter of 8.6 mm and a total height of 8.5 mm. It featured two concentric inner channels and a central linear channel for the accommodation of the Mg blades (Figure 6A). The concentric channels were located 4 and 1.9 mm from the center of the holder, each with a width of 0.5 mm. The MN holder was designed to house six Mg blades (30 MNs in total).

Methods—Mg MN Array Fabrication: For the fabrication of the MN array, 6 Mg blades (prepared as described in Mg blade fabrication and ex vivo assessment of MN penetration force) were manually bent around stainless-steel cylinders (d = 2 and d = 1 mm) and inserted into the channels of the holder (FDM fabrication of PLA MN holder and adapter). Thereafter, they were glued using a UV-curable glue (Permabond UV and Visible Light Cure Adhesive, Permabond Engineering Adhesives Ltd) and cured under UV light for 10 min. Note that to accomodate all 30 MN in the holder channels, one of the six blade was manually cut into two parts to retain 3 and 2 MNs, respectively.

Methods—Ex Vivo Skin Penetration Testing of Mg MN Array: MN arrays composed of 6 Mg blades (prepared as described in 4.2.18) were dipped in Tissue Marking Dye solution (blue) and dried for 2 h. To evaluate their skin penetration capability, the assembled MN patch was manually pressed on the freshly extracted porcine ear skin for a few seconds. After removal, excess dye from MN insertion sites was gently wiped away with distilled water, and the skin was imaged with an optical microscope (Leica MZ6 equipped with Flexcam C3, Leica Microsystems) to identify puncture marks. Afterward, to assess the penetration depth of the MNs, the punctured skin was embedded in OCT compound (Leica Microsystems), frozen, and sectioned into 20-µm slices using a cryostat (CryoStar NX50) at −18 °C. Sections were then thawed at RT for 30 min, and fixed in a 4% (w/v) methanol-free PFA solution in PBS for 10 min, followed by a 1-min wash in PBS and two rinses with distilled water. Slides were mounted using ProLong™ Diamond Antifade Mountant and covered with a coverslip. Cross-sectional images were acquired using a Leica DMI 6000 B microscope in brightfield mode.

Methods—PCL-Coating of Mg Blades and MN Patch: Before coating, Mg blades (200 µm thickness) were cleaned by immersion in 2 mL of acetone in a sonicator bath (Ultrasonic cleaner, Labmaterial or Bandelin Sonorex, Bandelin electronic) for 1 min to remove surface contaminants. The blades were then dried in an oven at 50 °C for 10 min. Coating was performed via dip-coating using a 20% (w/v) PCL (MW ≈50,000 g mol^{-1}) solution in CH_2Cl_2. Each blade was partially held with tweezers and slowly immersed in the polymer solution for 10 s to ensure uniform wetting. Thereafter, blades were withdrawn slowly (to minimize capillary-driven accumulation of the coating polymer between adjacent MNs) and dried in an oven at 50 °C for 10 min. This process

was repeated six times to achieve the desired coating thickness. For handling purposes, the dip-coating was performed on one half of each blade at a time.

For the MN patch, the dip-coating was carried out after assembling the patch. As previously described, Mg blades were cleaned by immersion in 2 mL of acetone and sonicated for 1 min. The cleaned blades were then embedded into the FDM-printed circular PLA basin (Mg MN array fabrication), forming the assembled MN patch. The patch was subsequently dip-coated using the same protocol as above.

Methods—SEM Analysis: The morphology of the Mg blades during degradation, as well as of the coated Mg blades and MN patch, was analyzed using a Hitachi SU5000 field emission scanning electron microscope (SU5000 FE-SEM, Hitachi High-Tech Corporation) in secondary electron mode. Samples were mounted on aluminium stubs with conductive carbon cement (Leit-C, Plano GmbH). Surface and cross-sectional images were acquired at an acceleration voltage of 3–10 kV for morphology, and 10 kV for elemental analysis. Cross-sections of the coated Mg blades were prepared by scalpel cutting before imaging.

Methods—In Vitro Hemolysis Assay After Porcine Whole Blood Storage in the 3D-Printed Device: For the in vitro hemolysis assay, 3D-printed devices were washed twice by immersion in a 90:10 2–propanol–acetone mixture after post-curing at 50 °C for 5 min. Following washing, the devices were stored in a desiccator until use, typically within three weeks. The hemolysis assay was conducted using freshly collected porcine whole blood treated with oxalate anticoagulant (Schlachtbetrieb Zürich AG). 1 mL of whole blood was loaded into the storage compartment of the device. A custom-designed PLA lid, fabricated via FDM (Pro 2, Raise 3D Technologies, Inc.) with commercial PLA (SPECTRUM Filament PLA tough natural, 1.75 mm), was inserted to ensure airtight sealing. The fully assembled device, with the lid facing upward, was placed in a sealed plastic bag and stored at RT for up to 24 h. As a control, 1 mL of porcine whole blood was stored in a 2-mL Eppendorf tube under identical conditions. To reduce the number of devices required, the following methodology was used. Specifically, at predefined time points (0, 10 min, 1, 3, 5, 7, and 24 h), the bag was opened, the lid removed, and 200 µL of blood were extracted from the device. The sample was centrifuged at 1000 × *g* for 10 min to separate plasma from red blood cells. After each sampling, 200 µL of fresh blood were reintroduced into the storage compartment to maintain a constant volume. It needs to be mentioned that this approach may lead to an underestimation of the hemolysis level. All blood and plasma samples were subsequently frozen until analysis. Hemolysis was quantified using a colorimetric Hb assay kit (Abcam, ab234046). A standard curve was generated over a concentration range of 0–100 mg dL^{-1}. To quantify the Hb concentration in the porcine blood, blood samples were diluted 1:20 (v/v). Plasma aliquots, instead, were analyzed without dilution. Specifically, 20 or 40 µL of each plasma sample were transferred to a 96-well plate, followed by the addition of 180 or 160 µL of Hb detection reagent, respectively. Percent hemolysis was calculated according to Equation (6):

$$\%\ Hemolysis = \frac{Hb\ conc\ in\ the\ plasma\ \ sample}{Total\ Hb\ concentration\ \ in\ whole\ blood} \times 100 \quad (6)$$

Methods—Blood Stability Study and Swelling of 3D-Printed Dog-Bone Specimens: 3D-printed poly(CL-LA)-MA dog-bone specimens were washed twice by immersion in a 90:10 (v/v) 2-propanol–acetone mixture at 50 °C for 5 min following post-curing. After washing, samples were stored in a desiccator until use, typically within three weeks. For the blood stability test, each specimen was immersed in 2 mL of freshly extracted porcine whole blood in an Eppendorf tube. At predefined time points (0, 10 min, 1, 3, 5, and 24 h), the strips were removed, quickly rinsed in distilled water, tapped with wipes, and the weight recorded. Swelling (%) was calculated using Equation (7):

$$\%\ Swelling = \frac{wt_{t-}wt_{t=0}}{wt_{t=0}} \times 100 \quad (7)$$

where $wt_{t=0}$ is the dry weight of the 3D-printed strip, and wt_t is the weight at the specified time point. Additionally, the pH of the blood was measured at each time point during the test using a Mettler Toledo pH electrode connected to an Orion Dual Star pH/ISE Meter.

Methods—In Vitro Hemolysis Assay of Porcine Whole Blood After Mg Blade Immersion: The in vitro hemolytic potential of Mg blades was assessed for both uncoated and coated Mg blades, prepared as described in Mg blade fabrication and ex vivo assessment of MN penetration force and PCL-coating of Mg blades and MN patch. For the assay, 1 mL of freshly collected porcine whole blood treated with oxalate (Schlachtbetrieb Zürich AG) was transferred into 2 mL Eppendorf tubes. Coated and uncoated Mg blades were immersed in separate Eppendorf tubes, while tubes containing only whole blood served as controls. To reduce the number of Mg blades required, the following methodology was used. Specifically, at predefined time points (0, 10 min, 1, 3, 5, 7, and 24 h), 200 µL of blood were withdrawn and centrifuged at 1000 × *g* for 10 min to isolate plasma. An equal volume of fresh blood was added after each sampling. Even in this case, this approach may still result in an underestimation of hemolysis levels. Hb concentrations in both whole blood and plasma samples were quantified using the same colorimetric assay described in in vitro hemolysis assay after porcine whole blood storage in the 3D-printed device. Whole blood samples were diluted 1:20 (v/v) prior to analysis, while plasma samples were measured without dilution. Additionally, blood pH was monitored over time (Mettler Toledo pH electrode connected to an Orion Dual Star pH/ISE Meter).

Methods—Prototype Assembling: To assemble the degradable prototype, the PCL-coated Mg MN patch (prepared as described in PCL-coating of Mg blades and MN patch) was glued to the inner top center of the printed device using a cyanoacrylate glue (Permabond 2050 Flexible superglue, Permabond Engineering Adhesives Ltd). The bottom rim of the device was then treated with a small amount of Permabond POP primer (polyolefin primer, Permabond Engineering Adhesives Ltd) to promote adhesion of the PLA adapter, which was subsequently bonded using the same cyanoacrylate glue. Following assembly, 150 µL of a 1% (w/v) K_2-EDTA solution prepared in a 1:1 (v/v) mixture of ethanol and distilled water was added to the device's storage compartment and allowed to dry overnight in a desiccator. Finally, an ECG was affixed to the underside of the device using fresh silicone adhesive (Sil-Poxy/0 Silicone Adhesive). The assembled device was stored in the desiccator until further use.

Methods—Ex Vivo Skin Puncturing Experiments with the Assembled Prototype: To assess the ability of the MNs to penetrate the skin, the assembled device—consisting of dye- (Tissue Marking Dye solution, blue) and PCL-coated MN patch and the PLA plate as described in Prototype assembling —was manually applied to freshly excised porcine ear skin for ≈10 s. Following removal, excess dye from MN insertion was rinsed off with distilled water, and the skin was imaged using an optical microscope (Leica MZ6 equipped with Flexcam C3) to visualize residual puncture sites. The subsequent steps to determine penetration depth followed the same protocol as previously described for the MN patch alone (ex vivo skin penetration testing of Mg MN array). Briefly, the punctured skin was embedded in OCT compound (Leica Microsystems), cryosectioned into 20-µm slices at −18 °C using a cryostat (CryoStar NX50), and fixed in a 4% (w/v) PFA solution. The sections were then mounted with ProLong™ Diamond Antifade Mountant, covered with a coverslip, and imaged in brightfield mode using a Leica DMI 6000 B microscope.

Methods—Ex Vivo Histological Evaluation of the Porcine Ear Skin After Prototype Application: Microscope slides (ex vivo skin puncturing experiments with the assembled prototype) were thawed for 30 min at RT. Subsequently, they were fixed using a 4% (w/v) PFA solution and subjected to the H&E staining procedure as described above. Cross-sectional images were recorded using the Leica DMI 6000 B microscope and light source (EL6000 mercury metal halide bulb, Leica Microsystems) with adaptive focus control at a magnification of ×10 (HC PL FLUOTAR L 20×, with correction collar, numerical aperture: 0.4, dry, Leica Microsystems) using LAS X Software (Leica Microsystems) in the tile scan mode (manual and automatic focusing; range, 60 µm) and were merged afterward. Images were

detected by a monochrome D FC365FX digital camera (12 bits, 1 × 1 BIN, Leica Microsystems).

Methods—Statistical Analysis: All data are presented as mean ± SD, mean + SD, or mean − SD, as specified in each figure caption. GraphPad Prism (version 10, GraphPad Software) was used for statistical analysis. For comparison of more than two groups, one-way analysis of variance (ANOVA) with Tukey's multiple comparison test was used. For comparison of more than two groups with two variables involved, two-way ANOVA with Tukey's multiple comparison test was used. A p-value < 0.05 was considered significant (visualized by $^{*}p < 0.05$, $^{**}p < 0.01$, $^{***}p < 0.001$, $^{****}p < 0.0001$).

Supporting Information

Supporting Information is available from the Wiley Online Library or from the author.

Acknowledgements

The authors thank Mr. Urs Notter from the mechanical workshop of the Physics Department at ETH Zürich for the fabrication of Mg blades using nitrogen laser cutting. Hwangseok Kim and Eunsong Jung from the laboratory of Prof. Dr. Tae-Lim Choi (ETH Zürich) are acknowledged for their assistance with SEC experiments. The authors also thank Dr. Gabriella Èva Bodizs from the Scientific Center for Optical and Electron Microscopy (ScopeM), Department of Health Sciences and Technology, ETH Zürich, for her support and assistance with H&E staining. Funding was provided by the Basel Research Centre for Child Health as part of the Postdoctoral Excellence Programme/Call for Essential Paediatric Medical Devices.

Conflict of Interest

The authors declare no conflict of interest

Data Availability Statement

The data that support the findings of this study are openly available in ETH research collection at https://www.research-collection.ethz.ch/.

Keywords

3D printing, capillary blood sampling, compostable device, magnesium microneedles, medical waste reduction

Received: July 31, 2025
Revised: September 15, 2025
Published online: October 6, 2025

[1] P. Xue, L. Zhang, Z. Xu, J. Yan, Z. Gu, Y. Kang, *Appl. Mater. Today* **2018**, *13*, 144.
[2] G. Lima-Oliveira, G. Lippi, G. L. Salvagno, G. Picheth, G. C. Guidi, *J. Med. Biochem.* **2015**, *34*, 288.
[3] L. S. Uman, K. A. Birnie, M. Noel, J. A. Parker, C. T. Chambers, P. J. McGrath, S. R. Kisely, *Cochrane Database of Syst. Rev.* **2013**, *10*, CD005179.
[4] B. Aykanat Girgin, İ. Göl, *Pain Manag. Nurs.* **2020**, *21*, 276.
[5] B. U. W. Lei, T. W. Prow, *Biomed. Microdevices* **2019**, *21*, 81.
[6] M. O. Harhay, S. D. Halpern, J. S. Harhay, P. L. Olliaro, *Trop. Med. Int. Health* **2009**, *14*, 1414.
[7] M. Caniato, T. Tudor, M. Vaccari, *J. Environ. Manag.* **2015**, *153*, 93.
[8] F. M. Nsubuga, M. S. Jaakkola, *Trop. Med. Int. Health* **2005**, *10*, 773.
[9] K. K. Padmanabhan, D. Barik, in *Energy from Toxic Organic Waste for Heat and Power Generation*, Elsevier, Amsterdam, Netherlands, **2019**, pp. 99–118.
[10] https://www.who.int/news-room/fact-sheets/detail/health-care-waste, (accessed: May 2025).
[11] M. N. Huda, T. G. Hailemariam, S. Z. Hossain, J. S. Malo, S. Khan, S. Hadisuyatmana, A. Ferdous, B. Akombi-Inyang, R. M. Islam, A. M. N. Renzaho, *BMJ Open* **2022**, *12*, 056037.
[12] M. Kermode, *Health Promot. Int.* **2004**, *19*, 95.
[13] P. B. Luppa, C. Müller, A. Schlichtiger, H. Schlebusch, *Trends Analyt. Chem.* **2011**, *30*, 887.
[14] V. Gubala, L. F. Harris, A. J. Ricco, M. X. Tan, D. E. Williams, *Anal. Chem.* **2012**, *84*, 487.
[15] M. M. Bond, R. R. Richards-Kortum, *Am. J. Clin. Pathol.* **2015**, *144*, 885.
[16] L. N. W. Daae, S. Halvorsen, P. M. Mathisen, K. Mironska, *Scand. J. Clin. Lab. Invest.* **1988**, *48*, 723.
[17] T. M. Blicharz, P. Gong, B. M. Bunner, L. L. Chu, K. M. Leonard, J. A. Wakefield, R. E. Williams, M. Dadgar, C. A. Tagliabue, R. El Khaja, S. L. Marlin, R. Haghgooie, S. P. Davis, D. E. Chickering, H. Bernstein, *Nat. Biomed. Eng.* **2018**, *2*, 151.
[18] L. D. Noble, C. Dixon, A. Moran, C. Trottet, M. Majam, S. Ismail, V. T. Msolomba, K. Mathobela, A. Queval, J. George, L. E. Scott, W. S. Stevens, *Diagnostics* **2023**, *13*, 1754.
[19] M. N. Fedoruk, *Bioanalysis* **2020**, *12*, 715.
[20] M. Protti, E. Milandri, R. Di Lecce, L. Mercolini, R. Mandrioli, *Adv. Sample Prep.* **2025**, *13*, 100161.
[21] N. Zoratto, D. Klein-Cerrejon, D. Gao, T. Inchiparambil, D. Sachs, Z. Luo, J. Leroux, *Adv. Sci.* **2024**, *11*, 2308809.
[22] E. Moshkbid, D. E. Cree, L. Bradford, W. Zhang, *J. Compos. Sci.* **2024**, *8*, 342.
[23] B. Joseph, J. James, N. Kalarikkal, S. Thomas, *Adv. Ind. Eng. Polym. Res.* **2021**, *4*, 199.
[24] A. H. Ainul Hafiza, M. K. Khairunnisa-Atiqah, N. S. N. Mazlan, K. M. Salleh, S. Zakaria, in *Green Sustainable Process for Chemical and Environmental Engineering and Science*, Elsevier, Amsterdam, Netherlands, **2023**, pp. 331–358.
[25] M. Hussain, S. M. Khan, M. Shafiq, N. Abbas, *Giant* **2024**, *18*, 100261.
[26] J. Rydz, W. Sikorska, M. Kyulavska, D. Christova, *Int. J. Mol. Sci.* **2014**, *16*, 564.
[27] V. DeStefano, S. Khan, A. Tabada, *Eng. Regen.* **2020**, *1*, 76.
[28] M. Puthumana, P. Santhana Gopala Krishnan, S. K. Nayak, *Int. J. Polym. Anal. Ch.* **2020**, *25*, 634.
[29] N. Paunović, Y. Bao, F. B. Coulter, K. Masania, A. K. Geks, K. Klein, A. Rafsanjani, J. Cadalbert, P. W. Kronen, N. Kleger, A. Karol, Z. Luo, F. Rüber, D. Brambilla, B. von Rechenberg, D. Franzen, A. R. Studart, J.-C. Leroux, *Sci. Adv.* **2021**, *7*, abe9499.
[30] Y. Liu, Y. Zheng, X. Chen, J. Yang, H. Pan, D. Chen, L. Wang, J. Zhang, D. Zhu, S. Wu, K. W. K. Yeung, R. Zeng, Y. Han, S. Guan, *Adv. Funct. Mater.* **2019**, *29*, 1805402.
[31] G. Kumar, S. Preetam, A. Pandey, N. Birbilis, S. Al-Saadi, P. Pasbakhsh, M. Zheludkevich, P. Balan, *J. Magnes. Alloys* **2025**, *13*, 948.
[32] S. N., F. A. Kalva, M. Koç, *Next Materials* **2025**, *6*, 100295.
[33] N. Paunović, J.-C. Leroux, Y. Bao, *Polym. Chem.* **2022**, *13*, 2271.
[34] H. Krupke, N. Zoratto, L. Rabut, D. Gao, N. Paunović, D. Klein Cerrejon, B. Dehapiot, J.-C. Leroux, *J. Controlled Release* **2025**, *384*, 113947.
[35] V. Mathiowetz, N. Kashman, G. Volland, K. Weber, M. Dowe, S. Rogers, *Arch. Phys. Med. Rehabil.* **1985**, *66*, 69.
[36] E. Bossi, E. Limo, L. Pagani, N. Monza, S. Serrao, V. Denti, G. Astarita, G. Paglia, *Metabolites* **2024**, *14*, 46.
[37] S. Amukarimi, M. Mozafari, *Med. Comm* **2021**, *2*, 123.

[38] M. Weber, H. Steinle, S. Golombek, L. Hann, C. Schlensak, H. P. Wendel, M. Avci-Adali, *Front. Bioeng. Biotechnol.* **2018**, *6*, 99.
[39] A. R. Williams, *Biorheology* **1973**, *10*, 303.
[40] K. S. Adeyemo, A. O. Mbata, O. D. Balogun, *Int. J. Multidiscip. Res. Growth Eval.* **2021**, *2*, 893.
[41] A. A. Jairoun, S. S. Al-Hemyari, M. Shahwan, A. M. Al-Ghananeem, F. El-Dahiyat, S. Al-Salmi, Z. U. D. Babar, *J. Pharmaceutical Policy and Practice* **2025**, *18*, 2519137.
[42] A. Mochizuki, H. Kaneda, *Mater. Sci. Eng. C.* **2015**, *47*, 204.
[43] T. Kokubo, H. Kushitani, S. Sakka, T. Kitsugi, T. Yamamuro, *J. Biomed. Mater. Res.* **1990**, *24*, 721.